Anisotropic surface tension of buckled fluid membranes

Hiroshi Noguchi[*]

Institute for Solid State Physics, University of Tokyo, Kashiwa, Chiba 277-8581, Japan

Thin solid sheets and fluid membranes exhibit buckling under lateral compression. Here it is revealed that buckled fluid membranes have anisotropic mechanical surface tension contrary to solid sheets. Surprisingly, the surface tension perpendicular to the buckling direction shows stronger dependence on the projected area than that parallel to it. Our theoretical predictions are supported by numerical simulations of a meshless membrane model. This anisotropic tension can be used to measure the membrane bending rigidity. It is also found that phase synchronization occurs between multilayered buckled membranes.

I. INTRODUCTION

Buckling and crumpling of thin solid sheets and strips [1,2] are commonly seen in our daily life (e.g., for fruits [3], paper [4,5], and polyester film [6]) as well as on the molecular scale (e.g., for viruses [7] and atomistic graphene sheets [8]). The shapes produced by the buckling of elastic sheets have fascinated many physicists. In 1691, J. Bernoulli proposed the problem of a simple bent beam or rod "elastica," which led to the development of the calculus of variation and the elliptic function [9]. The curve on a plane for minimum bending energy $\int^L c^2 ds$ with constant total length L is expressed by elliptic functions, where c is the curvature and s is the arc length. The theory of elastica was recently extended to twisted rods to describe the shape of supercoiled DNAs [10] and it has been employed to draw smooth surfaces in computer graphics [11].

The buckling has been intensively investigated for Langmuir monolayers on air-water interface [12–17]. The buckling develops to collapse or fold of the monolayers into water. For a fluid membrane, the balance between gravity and membrane bending energy determines the buckling wavelength [12]. Recently, buckling transition was also observed in a fluid bilayer membrane in simulations [18–20]. For the bilayer membrane, the effects of gravitation and membrane dissolution to the supporting water are negligible. Thus, the bilayer membrane is a simpler system so it is suitable to study the buckling of fluid membranes in details.

Recently, the stress and torque tensors in fluid membranes were derived [21,22]. When the membrane is curved, the mechanical surface tension is anisotropic and deviated from the thermodynamic surface tension (energy to create a unit membrane area). For a tubular membrane, the axial stress is finite while the azimuth stress is zero.

In this paper, we report on the shape and surface tension of buckled fluid membranes using an analytical theory and numerical simulation. Since the shape of buckled membrane can be analytically derived, the anisotropy of the mechanical tensions can be investigated in details. Buckling is one of the triggers for breaking membranes. For example, under shear flow, the formation of multilamellar vesicles [23,24] is considered to be induced by

buckling instability [25]. Shear suppression of the thermal undulations of the membrane and the resulting reduction of the excess area induces buckling. Our study revealed that buckling produces large anisotropy in the mechanical surface tension. This anisotropy may play a role in the membrane stability.

II. SIMULATION METHOD

We employ a solvent-free meshless membrane model [20,26] to simulate buckling. The fluid membrane is represented by a self-assembled one-layer sheet of particles. The particles interact with each other via the potential $U = \varepsilon(U_{rep} + U_{att}) + k_\alpha U_\alpha$, which consists of a repulsive soft-core potential U_{rep} with a diameter σ, an attractive potential U_{att}, and a curvature potential U_α. The details of the model are given in the Appendix.

We simulate single- and multilayer fluid membranes by Brownian dynamics in the NVT ensemble with periodic boundary conditions in a rectangular box with side lengths L_x, L_y, and L_z. The buckling is chosen in the x direction. The buckling occurs in the longest wavelength L_x in the x direction. When L_x is gradually reduced, the buckled membrane with large amplitude keeps its direction along x axis even at $L_x < L_y$. The bending rigidity κ_{cv} of the membrane shows a linear dependence on the parameter k_α. We calculate κ_{cv} from the thermal undulations of the planar membrane [27]. Three typical bending rigidities are chosen for the simulations: $\kappa_{cv}/k_B T = 9 \pm 0.2$, 21 ± 0.5, and 44 ± 1 for $k_\alpha/k_B T = 5$, 10, and 20, respectively, where $k_B T$ is the thermal energy. The surface tensions are calculated using $\gamma_x = -P_{xx} L_z$ and $\gamma_y = -P_{yy} L_z$, with the diagonal components of the pressure tensor $P_{\alpha\alpha} = (N k_B T - \sum_i \alpha_i \frac{\partial U}{\partial \alpha_i})/V$ for $\alpha \in \{x, y, z\}$, since $P_{zz} \simeq 0$ for solvent-free models. The numerical errors are estimated from three or more independent runs.

III. SINGLE BUCKLED MEMBRANE

First, we consider the buckling of an isolated planar membrane. Figure 1 shows buckled membranes at small projected areas $A_{xy} = L_x L_y$. When the thermal undulations are neglected, the shape of the membrane is given by the energy minimum of the bending energy F_{cv} of the membrane
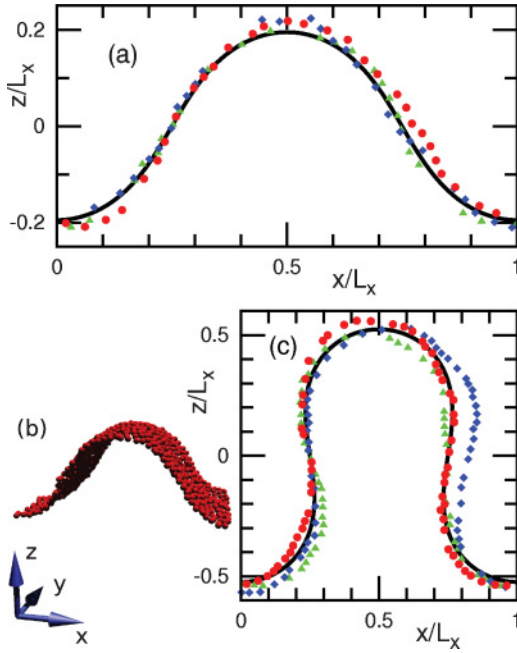
_____
[*]noguchi@issp.u-tokyo.ac.jp

FIG. 1. (Color online) Sliced shape of buckled fluid membranes at $L_x = 35\sigma$ and $\kappa_{cv} = 21k_BT$. (a) $A_{xy}/A = 0.75$, $L_y = 24\sigma$, and $N = 800$. (c) $A_{xy}/A = 0.375$, $L_y = 48\sigma$, and $N = 3200$. The solid curves are given by Eqs. (4) and (5). The closed symbols ($\bullet, \blacktriangle, \blacklozenge$) represent membrane particles in the simulation for three sequential sliced snapshots with time interval 2000τ. The curve and points are shifted in the x direction to overlap at $(x,z) = (0.25L_x, 0)$. (b) The 3D image of the simulated membrane shown with solid circles in (a).

with area constraints. For the buckled membrane, it is given by

$$F_{cv} = L_y \int_0^L \frac{\kappa_{cv}}{2}\left(\frac{d\theta}{ds}\right)^2 ds, \tag{1}$$

with constant intrinsic area $A = LL_y$, where s and θ are the arc length and the tangential angle on xz plane, respectively. When we consider the membrane compressed by a constant force λL_y in the x direction, it is an elastica problem to minimize $F_{total} = F_{cv} + \lambda L_x L_y$. Also, the force λL_y can be considered as a Lagrange multiplier to fix the length L_x. Euler's equation gives the shape equation

$$\frac{b^2}{2}\left(\frac{d\theta}{ds}\right)^2 = \cos(\theta) - \cos(\theta_{max}), \tag{2}$$

where the characteristic length $b = \sqrt{\kappa_{cv}/\lambda}$ and θ_{max} is the maximum tangential angle [9,10,28]. Then, the arc length s is written as $s = b\ F(\varphi,k)$, with $k = \sin(\theta_{max}/2)$ and $\sin(\theta/2) = k\sin(\varphi)$, where $F(\varphi,k)$ is the elliptic integral of the first kind with the elliptic modulus $0 \leqslant k \leqslant 1$ [29]. The modulus k is determined by the total arc length L from

$$\frac{L}{4b} = K(k), \tag{3}$$

where $K(k) = F(\pi/2,k)$ is the complete elliptic integral of the first kind. The shape of the buckled membrane is expressed by

$$x = 2b\ E[\text{am}(s/b,k),k] - s, \tag{4}$$

$$z = 2kb\ \text{cn}(s/b,k), \tag{5}$$

where $E(a,k)$, $\text{am}(a,k)$, and $\text{cn}(a,k)$ are the elliptic integral of the second kind, Jacobi amplitude, and Jacobi elliptic function, respectively [29]. Equations (4) and (5) reproduce the buckled shape of the simulation very well (see Fig. 1). The thermal fluctuations give small undulations of the simulated membrane around the energy minimum shape (solid curve). Strongly buckled membrane with $\theta_{max} > \pi/2$ ($k^2 > 1/2$) has a Ω shape as shown in Fig. 1(c). It is called class 4 of Euler's elastica [9].

Next, we derive the surface tension for fixed L_x and L_y using elliptic functions. We only consider the mechanical surface tension here. The modulus k is determined from the length ratio,

$$\frac{L_x}{L} = \frac{2E(k)}{K(k)} - 1. \tag{6}$$

The stress λ is a variable given by $\lambda = 16\kappa_{cv}[K(k)/L]^2$. The bending energy of the buckled membrane is given by

$$\begin{aligned}F_{cv} &= \lambda\{(2k^2 - 1)L + L_x\} \\ &= \frac{32\kappa_{cv}L_y}{L}\{(k^2 - 1)K(k)^2 - E(k)K(k)\}. \end{aligned} \tag{7}$$

The surface tensions in the x and y directions are given by

$$\gamma_x = \frac{\partial F_{cv}}{L_y \partial L_x}\bigg|_{L_y} = -\lambda, \tag{8}$$

$$\gamma_y = \frac{\partial F_{cv}}{L_x \partial L_y}\bigg|_{L_x} = -\lambda + \frac{2F_{cv}}{L_x L_y}, \tag{9}$$

respectively. The surface tension γ_x is balanced by the compressed stress λ as expected. However, the surface tension γ_y has the additional term $2F_{cv}/L_x L_y$. This anisotropy can also be derived from the stress tensor derived in Refs. [21,22]. In contrast, solid sheets show much weaker correlation between the x and y directions because of the shear elasticity.

The buckling transition points are obtained from the condition required to satisfy Eq. (3). Since $K(k) > K(0) = \pi/2$, it is written as $\lambda > \lambda_0 = (2\pi/L)^2\kappa_{cv}$ [9,28]. Therefore, the planar membrane becomes unstable at $\gamma = -(2\pi/L_x)^2\kappa_{cv}$. This result is in agreement with that estimated from the instability of the lowest Fourier mode of the thermal undulations [12,19,20]. This coincidence is not surprising because the elliptic function reduces to a trigonometric function at $k = 0$.

Figure 2 shows the surface tension dependence on A_{xy} for constant L_y. At $A_{xy} < A_{xy}^c = 1.4N\sigma^2$, the membrane is buckled, and then the two surface tensions γ_x and γ_y show different values. As A_{xy} decreases, it is found that γ_y increases, while γ_x shows a gradual decrease. Interestingly, the area decrease generates reduction of the counterstress in the y direction. It is surprising that γ_y becomes positive at $A_{xy}/N\sigma^2 < 0.9$ so that the buckled membrane prefers to shrink in the y direction. The average surface tension $\gamma_{av} = (\gamma_x + \gamma_y)/2$ also increases. These simulation results are
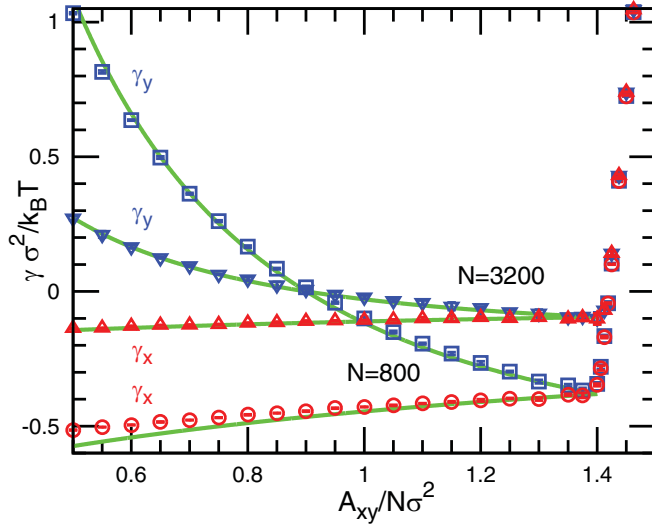
FIG. 2. (Color online) Area A_{xy} dependence of the surface tension for $\kappa_{cv} = 21k_BT$ and $L_y = 24\sigma$ ($N = 800$) or $L_y = 48\sigma$ ($N = 3200$). The symbols ($\circ, \triangle$) and ($\square, \nabla$) represent the surface tension γ_x and γ_y in the simulation, respectively. The solid lines are given by Eqs. (8) and (9).

in good agreement with our theoretical prediction given by Eqs. (8) and (9) with the area $A = A^c_{xy}$. The larger membrane starts buckling at smaller $\lambda = -\gamma$, and it has smaller A_{xy} dependence of γ_x and γ_y, since $\lambda_0 \propto L_x^{-2}$ (compare data for $N = 800$ and 3200 in Fig. 2).

When the aspect ratio L_y/L_x is fixed, the surface tensions show a different type of A_{xy} dependence (see Fig. 3). With decreasing A_{xy}, γ_x gradually increases, in contrast to its behavior for constant L_y, and the tension difference $\gamma_y - \gamma_x$ increases weakly. These effects are due to an increase in the arc length $L = A/L_y$ for the fixed aspect ratio. Thus, the surface tensions are dependent on the projected area as well as the aspect ratio.

When the aspect ratio L_y/L_x is allowed to change freely for a fixed projected area $A_{xy} = L_x L_y$, the membrane elongates in the x direction ($L_x \to \infty$) in order to reduce the membrane bending energy [$L_y/L \to 0$ with constant k in Eq. (7)]; that is, mechanically, the membrane pushes the wall in the buckled direction more than that in the other direction. This is a qualitative explanation of the anisotropic surface tension. Thus, the buckling gives the effective shear elasticity to the membrane.

For small buckling amplitude at $1 - A_{xy}/A^c_{xy} \ll 1$, the surface tensions can be expressed by polynomials. Equation (6) can be expanded to $L_x/L = 1 - k^2 - k^4/8 + o(k^6)$ for small k. From this relation and the expansions of Eqs. (8) and (9), the surface tensions are expressed as

$$\gamma_x = -\frac{\pi^2 \kappa_{cv}}{4L^2}\left(5 - \frac{L_x}{L}\right)^2, \tag{10}$$

$$\gamma_y - \gamma_x = \frac{8\pi^2 \kappa_{cv}}{L_x L}\left(1 - \frac{L_x}{L}\right). \tag{11}$$

The area dependence can be clearly captured by these equations. The surface tensions are determined by three quantities, $L_x/L = A_{xy}/A^c_{xy}$, A^c_{xy}, and κ_{cv}. These equations give a good
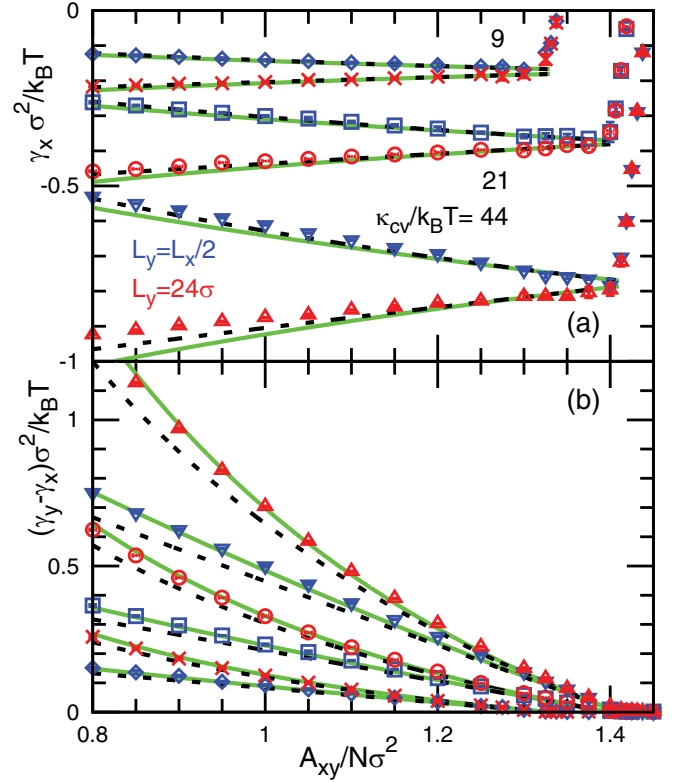

FIG. 3. (Color online) Area A_{xy} dependence of the surface tension for $\kappa_{cv}/k_BT = 9$, 21, or 44 and $N = 800$. The length L_x is varied with constant $L_y = 24\sigma$ ($\times, \circ, \triangle$) or constant ratio $L_y = L_x/2$ ($\diamond, \square, \nabla$). The solid lines are given by Eqs. (8) and (9). The dashed lines are given by the approximation, Eqs. (10) and (11).

approximation for $L_x/L \gtrsim 0.6$ (compare solid and dashed lines in Fig. 3).

Anisotropic surface tensions are also generated in a tubular membrane [30–32]. The surface tension in the axial direction is given by $\gamma_{ax} = \kappa_{cv}/R^2$, where R is the radius of the membrane tube; while the surface tension is zero in the azimuth direction. (The average surface tension $\gamma_{av} = \gamma_{ax}/2$.) The bending rigidity κ_{cv} of the membrane has been measured using this axial tension in experiments [30] and simulations [31]. Similarly, κ_{cv} can be measured from the surface tension of the buckled membrane. We fit the curves in Fig. 3(b) by Eq. (11) with the fit parameters κ_{cv} and A^c_{xy} for $0.05 < (A^c_{xy} - A_{xy})/N\sigma^2 < 0.3$. This gives $\kappa_{cv}/k_BT = 9.4 \pm 0.3$ (9.3 ± 0.3), 22.3 ± 0.1 (22.9 ± 0.2), and 47.4 ± 0.1 (48.4 ± 0.2) for constant L_y (constant ratio L_y/L_x) at $k_\alpha/k_BT = 5$, 10, and 20, respectively. These values are in reasonable agreement with the bending rigidities estimated from the thermal undulations of the planar membranes. Compared to the tubular membrane, this simulation method is easy to apply to explicit solvent systems and bilayer membranes with low flip-flop frequency. In the buckling, the area difference between the upper and the lower leaflets of bilayers are not changed, since the membrane deformation is symmetric. The solvent is not enclosed by the membrane, so the solvent volume is conserved when the volume of the simulation box is fixed. In contrast, a radius variation of the tubular membrane accompanies changes in the tube volume and the area difference between the two leaflets.
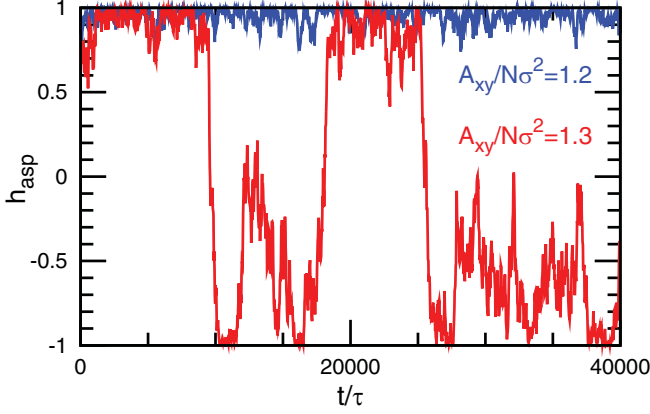
FIG. 4. (Color online) Time development of the aspect ratio h_{asp} of the buckled amplitude for $A_{xy}/N\sigma^2 = 1.2$ and 1.3 at $\kappa_{\text{cv}}/k_B T = 21$, $L_x = L_y$, and $N = 1600$.

Therefore, it has to take the Laplace pressure into account or requires an additional numerical technique to exchange the solvent particles or lipids between the upper and the lower sides of the bilayers. The new buckling method is suitable for measuring the bending rigidity of these membranes.

We neglect the effects of thermal fluctuations in our analysis. The excess area induced by the thermal undulations shows a slight increase with deceasing area in the buckling simulation. However, this does not have a large effect on the surface tensions. For a squared membrane $L_x = L_y$, the thermal fluctuations can induce a flip between the buckling in the x and y directions slightly below the buckling transition point. In the meshless membrane at $L_x = L_y$ and $N = 1600$,
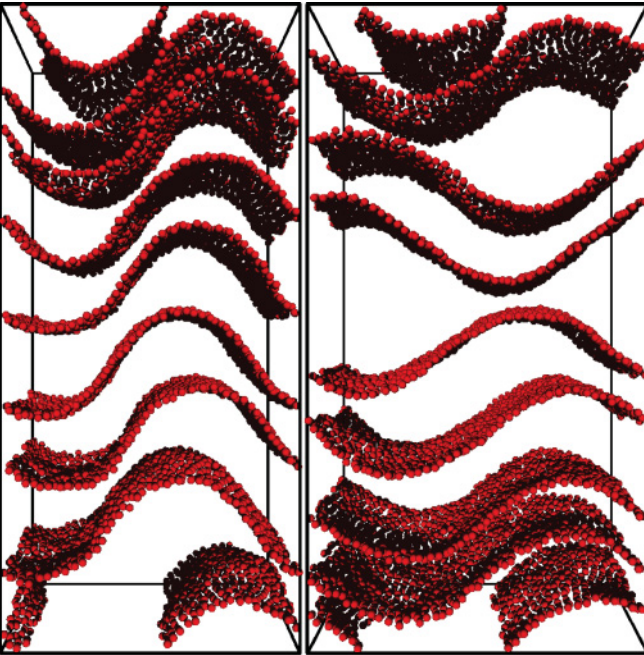
this flip is observed for $A_{xy}/N\sigma^2 \gtrsim 1.3$. Figure 4 shows the time development of the aspect ratio of the buckled amplitude,

$$h_{\text{asp}} = \frac{|h(q_{x1})|^2 - |h(q_{y1})|^2}{|h(q_{x1})|^2 + |h(q_{y1})|^2}, \tag{12}$$

where $h(q_{x1}) = \sum_j z_j \exp(-2\pi i x_j/L_x)$ and $h(q_{y1}) = \sum_j z_j \exp(-2\pi i y_j/L_y)$. The membrane changes the buckling direction at $A_{xy}/N\sigma^2 = 1.3$, while not at $A_{xy}/N\sigma^2 = 1.2$.

IV. MULTIPLE BUCKLED MEMBRANES

The membrane thermal undulations generate entropic repulsive force $f \propto d^{-3}$ between tensionless fluid membranes with neighboring membrane distance d [33]. Here we consider the interactions between the buckled membranes. Since the buckled membranes have greater height amplitudes than the tensionless membrane, the membranes have stronger short-range repulsion with decreasing area A_{xy} (see Fig. 5). Then, the fluctuation amplitude of the neighboring membrane distance $\langle (d/d_m - 1)^2 \rangle$ decreases for the fixed mean distance $d_m = L_Z/N_{\text{mb}}$, where N_{mb} is the number of the membranes [see the dashed line in Fig. 6(a)].

Along with this reduction in the distance fluctuation, it is found that the buckling of the neighboring membrane becomes synchronized in phase. The phase ϕ is calculated
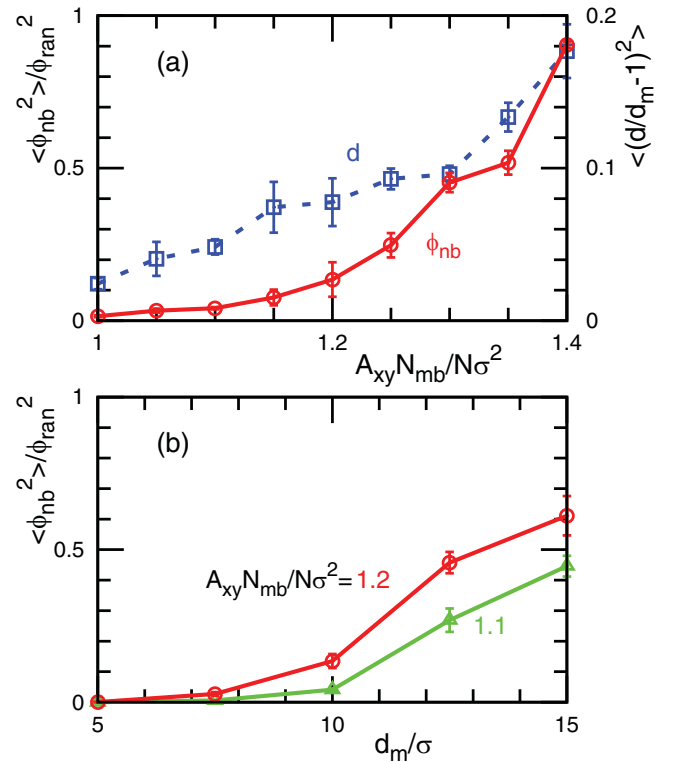

FIG. 6. (Color online) Phase synchronization of buckled membranes at $N = 6400$, $N_{\text{mb}} = 8$, $L_y/\sigma = 24$, and $\kappa_{\text{cv}}/k_B T = 21$. (a) The area A_{xy} dependence of the fluctuation amplitudes of the distance $\langle (d/d_m - 1)^2 \rangle$ ($\square$) and the phase difference $\langle \phi_{\text{nb}}^2 \rangle$ ($\circ$) between neighboring membranes at $d_m/\sigma = 10$. (b) The phase difference $\langle \phi_{\text{nb}}^2 \rangle$ dependence on the mean distance d_m between neighboring membranes at $A_{xy}N_{\text{mb}}/N\sigma^2 = 1.1$ ($\triangle$) and 1.2 ($\circ$).

FIG. 5. (Color online) Snapshots of multiple buckled membranes at $N = 6400$, $N_{\text{mb}} = 8$, $L_y/\sigma = 24$, $\kappa_{\text{cv}}/k_B T = 21$, and $d_m/\sigma = 10$. Left and right panels show the membranes with complete and partial phase synchronization at $A_{xy}N_{\text{mb}}/N\sigma^2 = 1.1$ and 1.25, respectively.

from the lowest Fourier mode of the membrane height, $h(q_{x1}) = h_{am} \exp(-i\phi) = \sum_j z_j \exp(-2\pi i x_j/L_x)$, for each membrane. The phase difference ϕ_{nb} between neighboring membranes approaches zero as A_{xy} decreases. The phase deviation of the neighboring membrane $\langle \phi_{nb}^2 \rangle / \phi_{ran}^2$ is shown as a solid line in Fig. 6(a), where ϕ_{nb}^2 is normalized by the average for the random distribution, $\langle \phi_{nb}^2 \rangle = \phi_{ran}^2 = \pi^2/3$. Thus, the translational order of the buckled shape appears in the z direction. This ordering is not a discrete transition but a gradual change, since it is a quasi-one-dimensional system. As A_{xy} decreases, clusters of the synchronized membrane appear, and then all of membranes are synchronized at $A_{xy} N_{mb}/N\sigma^2 \leqslant 1.1$. (see the snapshots in Fig. 5 and movies in the supplemental material [34]). The interactions between the membranes little change their surface tension in the simulated area range. As the mean distance d_m increases, the synchronization requires smaller A_{xy} [see Fig. 6(b)]. This synchronized buckling may act as a nucleus to form multilamellar vesicles in shear flow.

V. SUMMARY

We studied the elastica of fluid membrane. The buckled shape and surface tension parallel to the buckling (x) direction are expressed by the formula used for the elastica of solid sheets. However, unlike the solid sheets, the surface tension of the fluid membranes in the perpendicular (y) direction shows large increases for decreasing projected area A_{xy}. Additionally, multilamellar buckled membranes were found to have phase synchronization.

The anisotropic surface tension would also appear for the buckled Langmuir monolayers in the fluid phase. It can be experimentally checked, if one separately measures the stress in two lateral directions. The anisotropy and synchronization may play a role in the breakup of the membrane under external fields. Recent experiments show that collagen-containing tubular vesicles exhibit elastica shape under magnetic field [35]. It will be interesting to investigate the coupling of mechanical and external-field induced bucklings.

APPENDIX: DETAILS OF SIMULATION MODEL AND METHOD

A membrane consists of N particles, which possess no internal degrees of freedom. The particles interact with each other via a potential

$$U = \varepsilon(U_{rep} + U_{att}) + k_\alpha U_\alpha, \tag{A1}$$

which consists of a repulsive soft-core potential U_{rep} with a diameter σ, an attractive potential U_{att}, and a curvature potential U_α. All three potentials only depend on the positions $\mathbf{r}_i$ of the particles. In this paper, we employ the curvature potential based on the first-order moving least-squares (MLS)

method (model II in Ref. [20]). We briefly outline here the simulation technique, since the membrane model is explained in more detail in Ref. [20].

1. Curvature potential

A Gaussian function with C^∞ cutoff [20] is employed as a weight function

$$w_{mls}(r_{i,j}) = \begin{cases} \exp\left(\frac{(r_{i,j}/r_{ga})^2}{(r_{i,j}/r_{cc})^n - 1}\right) & (r_{i,j} < r_{cc}), \\ 0 & (r_{i,j} \geqslant r_{cc}), \end{cases} \tag{A2}$$

where $r_{i,j}$ is the distance between particles i and j. This function is smoothly cut off at $r_{i,j} = r_{cc}$. We use here the parameters $n = 12$, $r_{cc} = 3\sigma$, and $r_{ga} = 1.5\sigma$.

The degree of deviation from a plane, "aplanarity" is defined as

$$\alpha_{pl} = \frac{9D_w}{T_w M_w} = \frac{9\lambda_1\lambda_2\lambda_3}{(\lambda_1 + \lambda_2 + \lambda_3)(\lambda_1\lambda_2 + \lambda_2\lambda_3 + \lambda_3\lambda_1)}, \tag{A3}$$

where λ_1, λ_2, and λ_3 are the eigenvalues of the weighted gyration tensor, $a_{\alpha\beta} = \sum_j (\alpha_j - \alpha_G)(\beta_j - \beta_G) w_{mls}(r_{i,j})$, where $\alpha, \beta = x, y, z$ and $\mathbf{r}_G = \sum_j \mathbf{r}_j w_{mls}(r_{i,j}) / \sum_j w_{mls}(r_{i,j})$. The aplanarity can be calculated from three invariants of the tensor: D_w and T_w are determinant and trace, respectively, and M_w is the sum of its three minors, $M_w = a_{xx}a_{yy} + a_{yy}a_{zz} + a_{zz}a_{xx} - a_{xy}^2 - a_{yz}^2 - a_{zx}^2$.

The aplanarity α_{pl} takes values in the interval $[0,1]$ and represents the degree of deviation from a plane. This quantity acts like λ_1 for $\lambda_1 \ll \lambda_2, \lambda_3$, since $\alpha_{pl} \simeq 9\lambda_1/(\lambda_2 + \lambda_3)$ in this limit. Therefore, we employ the curvature potential

$$U_\alpha = \sum_i \alpha_{pl}(\mathbf{r}_i), \tag{A4}$$

where $\alpha_{pl}(\mathbf{r}_i) = 0$ when the ith particle has two or less particles within the cutoff distance $r_{i,j} < r_{cc}$. This potential increases with increasing deviation of the shape of the neighborhood of a particle from a plane and favors the formation of quasi-two-dimensional membrane aggregates.

2. Attractive and repulsive potentials

The particles interact with each other in the quasi-two-dimensional membrane surface via the potentials U_{rep} and U_{att}. The particles have an excluded-volume interaction via the repulsive potential

$$U_{rep} = \sum_{i<j} \exp[-20(r_{i,j}/\sigma - 1) + B] f_{cut}(r_{i,j}/\sigma), \tag{A5}$$

with $B = 0.126$, and a C^∞-cutoff function [20]

$$f_{cut}(s) = \begin{cases} \exp\left\{A\left(1 + \frac{1}{(|s|/s_{cut})^n - 1}\right)\right\} & (s < s_{cut}), \\ 0 & (s \geqslant s_{cut}), \end{cases} \tag{A6}$$

is employed. All orders of derivatives of $f_{cut}(s)$ are continuous at the cutoff. In Eq. (A5), we use the parameters $n = 12$, $A = 1$, and $s_{cut} = 1.2$.

A solvent-free membrane requires an attractive interaction which mimics the "hydrophobic" interaction. We employ a potential U_{att} of the local density of particles,

$$\rho_i = \sum_{j \neq i} f_{cut}(r_{i,j}/\sigma), \qquad (A7)$$

with the parameters $n = 12$, $s_{half} = 1.8$, and $s_{cut} = 2.1$. The factor A in Eq. (A7) is determined such that $f_{cut}(s_{half}) = 0.5$, which implies $A = \ln(2)\{(s_{cut}/s_{half})^n - 1\}$. Here ρ_i is the number of particles in a sphere whose radius is approximately $r_{att} = s_{half}\sigma$. The potential U_{att} is given by

$$U_{att} = \sum_i 0.25 \ln[1 + \exp\{-4(\rho_i - \rho^*)\}] - C, \quad (A8)$$

where $C = 0.25 \ln\{1 + \exp(4\rho^*)\}$. For $\rho_i < \rho^*$, the potential is approximately $U_{att} \simeq -\rho_i$ and therefore acts like a pair potential with $U_{att} \simeq -\sum_{i<j} 2f_{cut}(r_{i,j}/\sigma)$. For $\rho_i > \rho^*$, this function saturates to the constant $-C$. Thus, it is a pairwise

potential with cutoff at densities higher than $\rho_i > \rho^*$. In this paper, we use $\varepsilon/k_B T = 4$ and $\rho^* = 6$.

3. Dynamics

The buckling of the membrane is simulated by Brownian dynamics (molecular dynamics with Langevin thermostat). The motion of particles is determined by the underdamped Langevin equations

$$m\frac{d^2\mathbf{r}_i}{dt^2} = -\frac{\partial U}{\partial \mathbf{r}_i} - \zeta \frac{d\mathbf{r}_i}{dt} + \mathbf{g}_i(t), \qquad (A9)$$

where m is the mass of a particle and ζ the friction constant. $\mathbf{g}_i(t)$ is a Gaussian white noise which obeys the fluctuation-dissipation theorem. We employ the time unit $\tau = \zeta\sigma^2/k_B T$ with $m = \zeta\tau$. The Langevin equations are integrated by the leapfrog algorithm [36,37] with a time step of $\Delta t = 0.005\tau$.

[1] T. A. Witten, Rev. Mod. Phys. **79**, 643 (2007).
[2] D. R. Nelson, T. Piran, and S. Weinberg, eds., *Statistical Mechanics of Membranes and Surfaces*, 2nd ed. (World Scientific, Singapore, 2004).
[3] J. Yin, Z. Cao, C. Li, I. Sheinman, and X. Chen, Proc. Natl. Acad. Sci. USA **105**, 19132 (2008).
[4] G. Domokos, W. B. Fraser, and I. Szeberényi, Phys. D **185**, 67 (2003).
[5] G. A. Vliegenthart and G. Gompper, Nat. Mater. **5**, 216 (2006).
[6] L. Pocivavsek, R. Dellsy, A. Kern, S. Johnson, B. Lin, K. Y. C. Lee, and E. Cerda, Science **320**, 912 (2008).
[7] J. Lidmar, L. Mirny, and D. R. Nelson, Phys. Rev. E **68**, 051910 (2003).
[8] V. M. Pereira, A. H. Castro Neto, H. Y. Liang, and L. Mahadevan, Phys. Rev. Lett. **105**, 156603 (2010).
[9] C. Truesdell, Bull. Am. Math. Soc. **9**, 293 (1983).
[10] H. Tsuru and M. Wadati, Biopolymers **25**, 2083 (1986).
[11] A. M. Bruckstein, R. J. Holt, and A. N. Netravali, Appl. Anal. **78**, 453 (2001).
[12] S. T. Milner, J. F. Joanny, and P. Pincus, Europhys. Lett. **9**, 495 (1989).
[13] M. M. Lipp, K. Y. C. Lee, J. A. Zasadzinski, and A. J. Waring, Science **273**, 1196 (1996).
[14] E. Hatta and J. Nagao, Phys. Rev. E **67**, 041604 (2003).
[15] Q. Zhang and T. A. Witten, Phys. Rev. E **76**, 041608 (2007).
[16] S. Baoukina, L. Monticelli, H. J. Risselada, S. J. Marrink, and D. P. Tieleman, Proc. Natl. Acad. Sci. USA **105**, 10803 (2008).
[17] L. Pocivavsek, S. L. Frey, K. Krishan, K. Gavrilov, P. Ruchala, A. J. Waring, F. J. Walther, M. Dennin, T. A. Witten, and K. Y. C. Lee, Soft Matter **4**, 2019 (2008).
[18] J. Stecki, J. Chem. Phys. **120**, 3508 (2004).
[19] W. K. den Otter, J. Chem. Phys. **123**, 214906 (2005).
[20] H. Noguchi and G. Gompper, Phys. Rev. E **73**, 021903 (2006).
[21] R. Capovilla and J. Guven, J. Phys. A: Math. Gen. **35**, 6233 (2002).
[22] J. B. Fournier and P. Galatola, Phys. Rev. Lett. **98**, 018103 (2007).
[23] O. Diat and D. Roux, J. Phys. II (France) **3**, 9 (1993).
[24] F. Nettersheim, J. Zipfel, U. Olsson, F. Renth, P. Lindner, and W. Richtering, Langmuir **19**, 3603 (2003).
[25] A. G. Zilman and R. Granek, Eur. Phys. J. B **11**, 593 (1999).
[26] H. Noguchi and G. Gompper, J. Chem. Phys. **125**, 164908 (2006).
[27] H. Shiba and H. Noguchi, e-print arXiv:1105.3098.
[28] M. Toda, *Introduction of Elliptic Function* (Nihonhyoron, Tokyo, 2001).
[29] P. F. Byrd and D. F. Morris, *Handbook of Elliptic Integrals for Engineers and Physicists* (Springer, Berlin, 1954).
[30] L. Bo and R. Waugh, Biophys. J. **55**, 509 (1989).
[31] V. A. Harmandaris and M. Deserno, J. Chem. Phys. **125**, 204905 (2006).
[32] J. B. Fournier, Soft Matter **3**, 883 (2007).
[33] W. Helfrich, Z. Naturforsch. **28c**, 693 (1973).
[34] See supplemental material at [http://link.aps.org/supplemental/10.1103/PhysRevE.83.061919] for snapshots in Fig. 5 and movies.
[35] K. Suzuki, T. Toyota, K. Sato, M. Iwasaka, S. Ueno, and T. Sugawara, Chem. Phys. Lett. **440**, 286 (2007).
[36] M. P. Allen and D. J. Tildesley, *Computer Simulation of Liquids* (Clarendon Press, Oxford, 1987).
[37] H. Noguchi, J. Chem. Phys. **134**, 055101 (2011).